Energy & Environmental Science

Super Stable Antimony-carbon Composite Anodes for Potassium-ion Batteries

Journal:	*Energy & Environmental Science*
Manuscript ID	EE-ART-09-2018-002836.R1
Article Type:	Paper
Date Submitted by the Author:	07-Dec-2018
Complete List of Authors:	Zheng, Jing; University of Maryland, College Park, Department of Chemical & Biomolecular Engineering Yang, Yong; University of Maryland at College Park A James Clark School of Engineering, Department of Chemical and Biomolecular Engineering Fan, Xiulin; University of Maryland, Department of Chemical & Biomolecular Engineering Ji, Guangbin; Nanjing University of Aeronautics and Astronautics, College of Material Science and Technology Ji, Xiao; Huazhong University of Science and Technology, School of Optical and Electronic Information Wang, Haiyang; University of Maryland, college park, Department of Chemical & Biomolecular Engineering Hou, Singyuk; University of Maryland, Department of Chemical & Biomolecular Engineering Zachariah, Michael; University of Maryland at College Park, Wang, Chunsheng; University of Maryland, Department of Chemical & Biomolecular Engineering

Super Stable Antimony-carbon Composite Anodes for Potassium-ion Batteries

Jing Zheng,[a,b,†] Yong Yang,[a,†] Xiulin Fan,[a] Guangbin Ji,[b] Xiao Ji,[a] Haiyang Wang,[a] Singyuk Hou,[a] Michael R. Zachariah[a,c,*] Chunsheng Wang[a,c,*]

[a] *Department of Chemical and Biomolecular Engineering University of Maryland, College Park, MD 20742, USA*

[b] *College of Materials Science and Technology, Nanjing University of Aeronautics and Astronautics, Nanjing 210016, P. R. China*

[c] *Department of Chemistry and Biochemistry, University of Maryland, College Park, MD 20742, USA*

* *Corresponding author, Prof. Chunsheng Wang, Tel.: 301.405.0352, Fax: 301.314.9216, E-mail: cswang@umd.edu;* Prof. Michael R. Zachariah, Tel.: 301.405.4311, Email: mrz@umd.edu

Abstract:

Potassium-ion batteries (PIBs) have been considered as promising alternatives to lithium-ion batteries due to the high natural K abundance of 2.09 wt.% (vs. 0.0017 wt.% for Li) and low K/K$^+$ redox potential of −2.93 V (vs. -2.71 V for Na/Na$^+$). However, PIB electrodes still suffer huge challenges due to the large K-ion radius and slow reaction dynamics. Herein, we report a high-capacity Sb@CSN composite anode with Sb nanoparticles uniformly encapsulated by carbon sphere network (CSN) for PIBs. First-principles computations and electrochemical characterizations confirm a reversible sequential phase transformation of KSb_2, KSb, K_5Sb_4, and K_3Sb during potassiation/depotassiation process. In a concentrated 4M KTFSI/EC+DEC electrolyte, the Sb@CSN anode delivers a high reversible capacity of 551 mAh/g at 100 mA/g for 100 cycles with an extremely slow capacity decay of only 0.06% per cycle from the 10th to 100th cycling; when up to a high current density of 200 mA/g, Sb@CSN anode still maintains a capacity of 504 mAh/g for 220 cycles. The Sb@CSN anodes demonstrate one of the best electrochemical performances for all K-ion batteries anodes reported to date. The exceptional performances of Sb@CSN should be attributed to the efficient capsulation of small Sb nanoparticles into conductive carbon network as well as the formation of a robust KF-rich SEI layer on Sb@CSN anode in the concentrated 4M KTFSI/EC+DEC electrolyte.

Keywords:

Potassium-ion battery; Concentrated electrolyte; Antimony-based anode; Stable SEI

Introduction

With the continuously increasing consumption of traditional nonrenewable energy sources along with severe global environmental issues, developing efficient and renewable energy storage technologies has been more urgently required. Lithium-ion batteries (LIBs) as efficient electrical energy storage technology has been successfully developed and widely used in various types of electronic devices and electric vehicles.[1, 2] However, the broad utilization of LIBs in large-scale energy storage systems is still significantly hindered by the limited and unevenly distributed availability of Li in the earth's crust (0.0017 wt.%).[3, 4] In the past decades, many efforts have been devoted to developing alternative batteries using earth-abundant and cheap materials. Recently, sodium-ion batteries (SIBs) and potassium-ion batteries (PIBs) have received increasing attention because of their high abundance (2.36 and 2.09 wt.% for Na and K, respectively) and low cost.[5] Especially for PIBs, its lower redox potential (−2.93 V) for K/K^+ than Na/Na^+ (−2.71 V vs. SHE) guarantees a higher operation voltage and higher energy density, making it as a promising candidate for high-energy-density and low-cost electrical energy storage applications.

Significant advances have been achieved in developing high-performance PIBs cathode materials such as amorphous $FePO_4$,[6] $FeSO_4F$,[7] Prussian blue,[8] Prussian Green,[9] and organic material[10]. The research on anode materials mainly focus on carbonaceous materials, such as hard carbon,[11] soft carbon,[12] graphite,[13, 14] and reduced graphene oxide[15]. However, these carbonaceous materials have a low capacity of less than 300 mAh/g. Metal anode through alloying/de-alloying reaction with K can provide a much higher specific capacity than that of intercalation type anode.[16] As a result, adding metal into carbon materials can significantly enhance the capacity of carbonaceous materials. Recently, Sn-carbon composite prepared by mechanical ball-milling of Sn powder with graphite was reported for PIBs. However, the capacity of Sn-C composite anode quickly drops from 288 mAh/g at 1st cycle to a low value of 150 mAh/g after 30th cycling even at a low current density of 25 mA/g.[17] Such rapid capacity decay is caused by the large volume change during alloy/de-alloy processes, which leads to obvious electrical disconnection between the electrode material and current collector.[18] Although encapsulation of Sn nanoparticles into carbon skeleton[19], mesoporous nanostructured carbon[20], or nanocrystalline materials[21] can migrate the damage from volume expansion/contraction during cycles, the capacity of Sn@C anodes is still declined during the charge/discharge cycles due to high mobility of Sn nanoparticles. Alternatively, antimony (Sb) with a low mobility has been investigated for PIBs anodes. As in Li-ion and Na-ion batteries,[22,23] Sb can also form K_3Sb[24] by reacting with K. However, Sb-based anode prepared by simply ball-milling of a mixture of carbon black and "bulk" antimony powder can only provide a capacity of 250 mAh/g for 50th cycles, similar to the Sn@C anode in PIBs.[25] Furthermore, electrolytes are also critical for stabilizing PIBs anodes because the nature of solid electrolyte interphase (SEI) layer on the anode significantly affects the cycling performance of PIBs.[26] However, to our best of knowledge, only limited study on the SEI design via rational electrolyte regulation have been reported.[27, 28] Therefore, in order to achieve a high capacity and excellent cycle stability for Sb-based K storage process, nanostructure improvements as well as electrolyte design should be concerned simultaneously.

Herein, a novel class of Sb-based composite is prepared via a scalable electrospray-assisted strategy. This approach enables Sb nanoparticles to be uniformly encapsulated by an interconnecting carbon sphere network (Sb@CSN), which not only works as a buffering matrix to mitigate the deleteriously mechanical damage from the large volume changes during alloy/de-alloy cycling, but also acts as a highly conductive framework for fast electron transport. More importantly, we also regulate the components of ester-based electrolytes to promote the formation of KF-rich SEI layer on Sb@CSN anode. Surprisingly, the Sb@CSN composite in the optimized 4M KTFSI/EC+DEC electrolyte delivers excellent reversible capacity of 551 mAh/g at 100 mA/g over 100 cycles with a low capacity decay of 0.06% per cycle from the 10th to 100th cycling and 504 mAh/g even at a high current density of 200 mA/g over 220 cycling. Sb@CSN composite anodes also show an excellent rate performance by providing high capacity of 589 mAh/g at 50 mA/g and still maintaining 530 mAh/g even at 200 mA/g. These outstanding performances should be attributed to the novel nanostructure of Sb nanoparticles uniformly encapsulated into conductive carbon network and the formation of a more stable and robust KF-rich SEI layer on Sb@CSN in the optimizd 4M KTFSI/EC+DEC electrolyte. To our best knowledge, the Sb@CSN composites in our work show one of the highest capacity and longest cycle life in all reported PIBs anodes to date.

Result and discussion

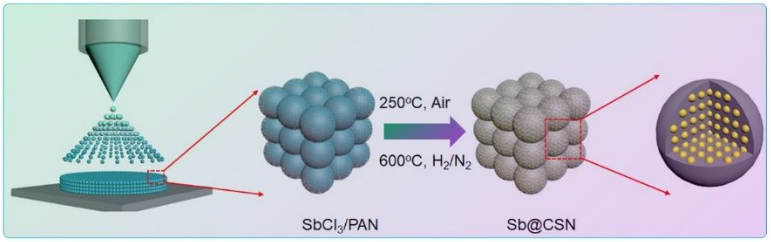

Scheme 1. Schematic illustration of electrospray-assisted strategy for fabricating Sb@CSN material.

Sb@CSN materials were synthesized using a scalable electrospray-assisted strategy, as illustrated in Scheme 1. Under the controllable high-voltage electrostatic field between the needle and the substrate collector, the precursor solution containing polyacrylonitrile (PAN) and $SbCl_3$ was nebulized to generate high concentrations of highly charged microdroplets when dried in free flight, which served as the primary building blocks for porous 3D network construction. The formed PAN nanospheres with evenly-distributed $SbCl_3$ (marked as $SbCl_3$/PAN) was collected from the substrate and then thermally stabilized and reduced to generate uniform metal Sb nanoparticles which were well confined into in-situ formed carbon spheres network (CSN) to obtain Sb@CSN material.

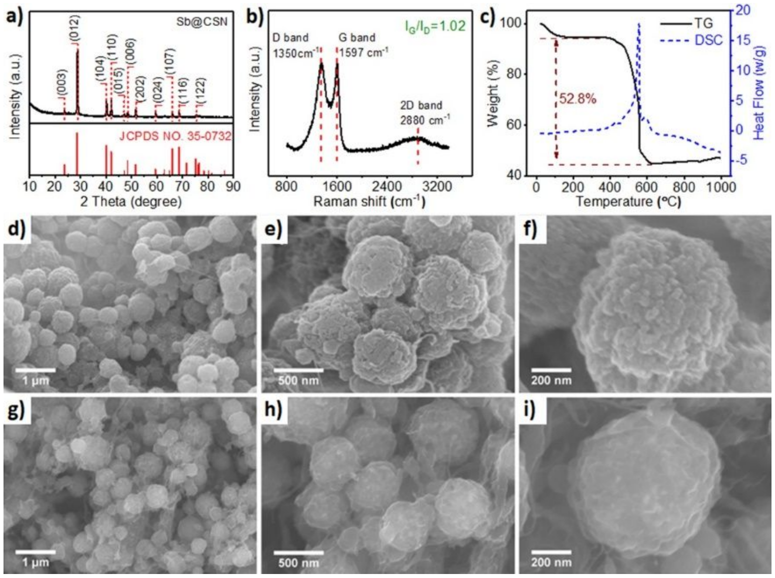

Figure 1 a) XRD pattern, b) Raman spectra, and c) TG-DSC curves for Sb@CSN material; SEM images of the d-f) as-prepared $SbCl_3$/PAN precursor and g-i) Sb@CSN composite.

Figure 1 demonstrates the structure and morphology of Sb@CSN composite material revealed by XRD, TG-DSC, Raman, and SEM analysis. As shown in Figure 1a, the XRD pattern of the Sb@CSN material is consistent with hexagonal Sb (JCPDS no. 35-0732), without any other phases or impurities, indicating that Sb^{3+} was reduced completely to metallic Sb during the synthesis process. Using the Scherrer equation to the (012) peaks of Sb, the average size of Sb crystallites was calculated at around 18 nm. On the other side, Raman spectrum was used to reveal the structure property of the carbon in Sb@CSN composites. The Raman spectrum in Figure 1b shows that the three bands at 1350, 1597, and 2880 cm^{-1}, corresponding to D, G and 2D bands; moreover, the intensity ratio between the G and D band (I_G/I_D) is 1.02, suggesting a high degree of graphitization for the carbon in Sb@CSN, which should offer better electro-conductivity.[29] To evaluate the content of Sb in the prepared Sb@CSN material, TG-DSC analysis was carried out in air from room temperature to 1000 ºC, as displayed in Figure 1c. The slight weight loss at around 100 ºC resulted from adsorbed solvent evaporation; the main weight loss at around 500 ºC is due to carbon oxidation. According to oxygen-antimony binary phase diagram (Figure S1a), a small peak in the DCS curve at around 590 ºC is attributed to the oxidation of Sb nanoparticles to form Sb_2O_4.[30] As a result, the mass loading of Sb for prepared Sb@CSN material can be calculated at around 37.8 wt.%.

The morphology of the $SbCl_3$/PAN precursor and Sb@CSN before and after heat treatment is shown in Figure 1d-f and Figure 1g-i, respectively. The as-prepared $SbCl_3$/PAN precursor in Figure 1d-f demonstrates uniform spheres which interconnect to form a three-dimensional (3D) network. Notably, these spheres have a crumpled surface, probably formed by the capillary compression during the solvent evaporation from the aerosol droplets.[31] This crumpled surface microstructure can be very beneficial for boosting the surface area of the carbon network. After carbonization, the obtained Sb@CSN maintains a similar microstructure and morphology, indicating that the unique structure of the prepared material can be maintained after the heat treatment. Figure 1g-i illustrates the interconnection between each primary carbon sphere embedded with secondary Sb nanoparticles (Figure S1b-c), which enables the continuous 3D conductive network to provide a fast electronic and ionic transfer path and effectively accommodate the volume changes.

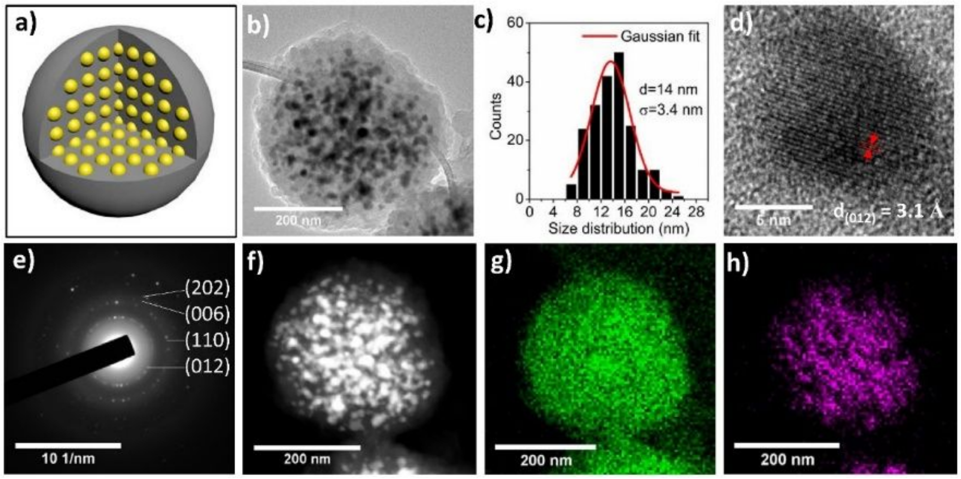

Figure 2 a) Schematic illustration of uniform Sb nanoparticles confined in a carbon sphere (Sb@CSN); b) TEM image of an individual Sb@CSN sphere and c) corresponding size distribution curve of Sb nanoparticles from image b); d) HRTEM image, e) selected-area electron diffraction pattern, and f-h) EDS images for one individual Sb@CSN sphere, g) for C and h) for Sb element.

The microstructure and morphology of Sb@CSN was also examined by TEM analysis, as shown in Figure 2. Figure 2a represents a schematic illustration of uniform Sb nanoparticles confined in a carbon sphere. The corresponding TEM image in Figure 2b indicates that the Sb nanoparticles are well-encapsulated and uniformly distributed in the carbon sphere. The size distribution curve in Figure 2c indicates a relatively narrow size distribution for Sb nanoparticles in prepared Sb@CSN material, with an average size of 14 nm and a standard deviation of 3.4 nm, which is consistent with the XRD results. The HRTEM image shown in Figure 2d suggests that the Sb nanoparticle has a good crystalline structure, confirmed by the 3.1Å distance of lattice fringes corresponding to the (012) plane of the metallic Sb. The selected-area electron diffraction pattern (SAD) in Figure 2e exhibits typical SAD pattern of metallic Sb. The lack of diffraction rings corresponding to Sb_2O_4 suggests that carbon matrix serves as an effective barrier to prevent the Sb nanoparticles from oxidizing. The element mapping images in Figure 2f-h suggests a uniform distribution of Sb nanoparticles in the carbon sphere matrix.

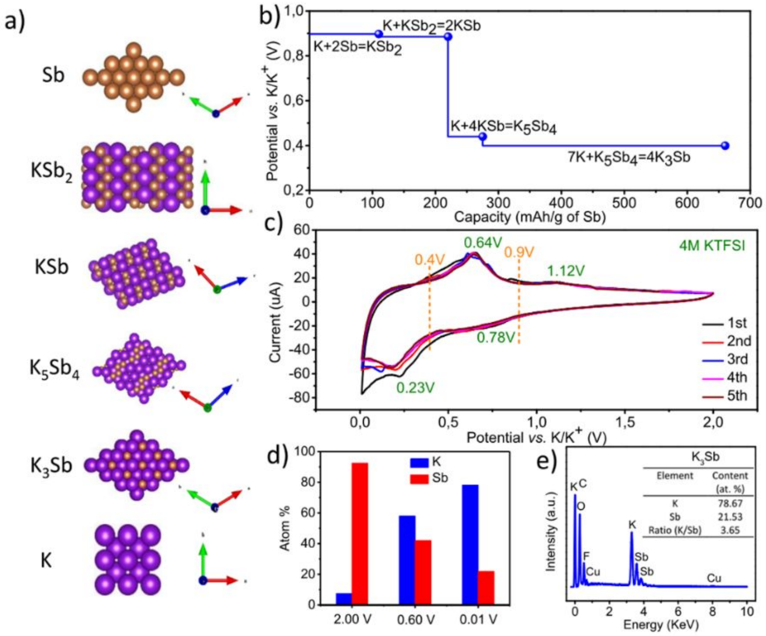

Figure 3 a) Crystal structure of K and stage structure evolutions from Sb to K_3Sb during potassiation process; b) DFT calculated equilibrium voltages (vs. K/K^+) for the potassiation process; c) CV curves for Sb@CSN electrode at scan rate of 0.05 mV/s; d) Relative atom% of K and Sb from EDS with different discharge cut-off voltage; e) EDS element analysis for K_3Sb with discharge cut-off voltage of 0.01 V. (Cells from d-f are all in 4M KTFSI electrolyte)

According to the potassium-antimony binary phase diagram (Figure S2a), there are four intermediate phases from KSb_2, KSb, K_5Sb_4 to K_3Sb along with the increasing of K content, and the corresponding crystalline structures are exhibited in Figure 3a. The equilibrium potential for the reaction process of K with Sb was obtained using first-principles computations based on density functional theory (DFT). As can be seen from Figure 3b, the thermodynamic equilibrium potentials of KSb_2 and KSb are 0.89 V and 0.849 V, respectively. Similarly, the two adjacent equilibrium potentials of K_5Sb_4 and K_3Sb are 0.439 V and 0.398 V, respectively. The K concentration in K_xSb interphases corresponds to the X= 0.5, 1.0, 1.25, and 3.0 with a theoretical capacity of 108, 216, 270, 660 mAh/g, occupying the total capacity percentage of 16.4%, 16.4%, 8.2%, and 59.1%, respectively. Furthermore, two prominent potential platforms can be clearly found in the calculated potential profile, corresponding to the equilibrium potentials of the above-mentioned interphases. A dramatic potential drop from around 0.9 V to 0.4 V when the capacity excess

216 mAh/g; subsequently, the potential profile slowly decreases from 0.439 V to 0.398 V, with the formation of K_3Sb.

Electrochemical behavior of Sb@CSN anode was evaluated using cyclic voltammetry (CV) at a scan rate of 0.05 mV/s in coin cells using K as counter electrode and 4M KTFSI/EC+DEC (abbreviated as "4M KTFSI") as electrolyte. As displayed in Figure 3c, two pairs of redox peaks at approximate 0.4 V and 0.9 V potentials can be observed in the CV curve during the alloying/de-alloying process, in consistence with the calculated intermediate K_xSb phases located at around 0.9 V and 0.4 V in Figure 3b. The alloying peak located at around 0.78 V in potassiation process should be attributed to the stepwise alloying reaction of Sb to form KSb_2/KSb. Furthermore, the similar equilibrium reaction voltage between these two intermediates leads to an appearance of the overlap broad peak at 0.78 V. Another reduction peak centered at about 0.23 V is also an overlap broad peak, which was resulted from the approximate formation voltage for both K^+ insertion in C and the step formation of K_5Sb_4 and K_3Sb alloys.[32] Based on the potential-capacity curve in Figure 3b, the formation of K_3Sb occupied a large proportion of theoretical capacity (58.5%), which is the reason why the peak at 0.23 V is larger than that of 0.78 V. The peaks voltage both at 0.78 V and 0.23 V are slightly lower than that of the corresponding value from theoretical calculation, which is primarily due to the overpotential. On the reversed anodic scan, there is a distinct anodic peak at 0.64 V and a minor oxidation peak at 1.12 V, which is due to the extraction reaction of K during depotassiation reaction. In similar manner, the peaks of K_3Sb and K_5Sb_4 overlap with each other to form a new broad apparent peak at 0.64 V but an inconspicuous peak of KSb and KSb_2 at 1.12 V. In the same situation of overpotential, these oxidation peaks gradually shifted to higher potentials when compared with the theoretical values. Owing to SEI film formation during the first cathodic scan, a lower current peak at the initial cycle is observed, slightly distinguished from subsequent cycles where the SEI layer has already formed.[33] However, after the second and subsequent reduction/oxidation scans, the CV curves keep stable in their shapes and current intensities. Therefore, the CV curves demonstrate that the Sb@CSN material can perform reversibly alloy/de-alloy reaction with K at potential region of 0.01-2.0 V.

Energy dispersive spectroscopy (EDS) elemental mapping was carried out to investigate the chemical composition of the formed interphases during charging/discharging process. Figure 3d shows the atomic percentages of K/Sb from the Sb@CSN electrode taken at different cut-off voltages (2.0, 0.6, and 0.01 V) during the 5th discharge process. The ratio of K/Sb can provide insight into the composition of the alloy interphase at each cut-off voltage. Obviously, along with the increasing discharge depth from 2 V to 0.01 V, the atomic ratio of K to Sb increases, indicating deeper K alloying reaction with Sb. Notably, the ratio of K/Sb maintains a constant value of 3.65 in EDS elemental mapping when the cut-off voltage is 0.01 V (Figure 3e), slightly higher than that of the K_3Sb, which is probably attributed to the unclean-washed potassium salt from the electrolyte. Furthermore, as shown in Figure S2b-f, the elements of C, K and Sb have an even distribution in nanometer scale among Sb@CSN electrode even at the highest discharge depth of 0.01 V.

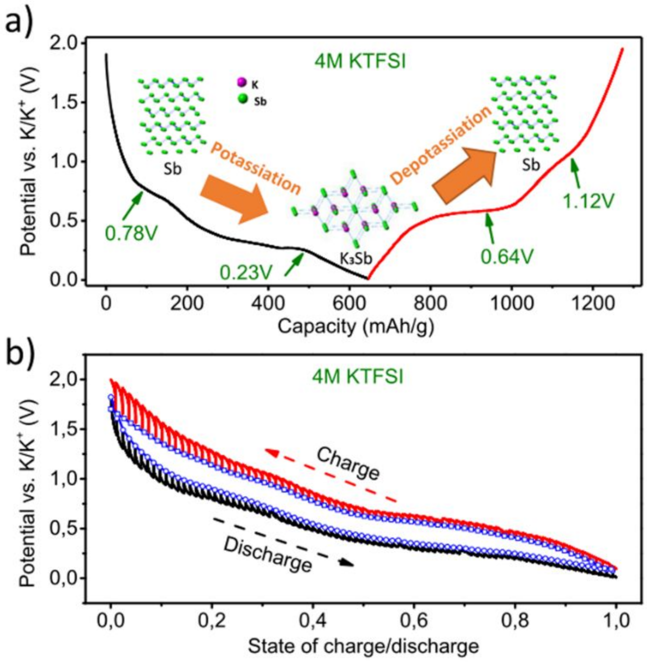

Figure 4 Electrochemical K storage properties for Sb@CSN in the 4M KTFSI electrolyte. a) Typical 2nd charge/discharge profile at 50 mA/g; b) quasi-equilibrium voltage profile from galvanostatic intermittent titration technique (GITT) at 100 mA/g.

Figure 4a shows the galvanostatic charge/discharge behavior of Sb@CSN in 4M KTFSI concentrated electrolyte at a low current density of 50 mA/g in the second cycle after the formation of SEI. The mass capacities of Sb were calculated by subtracting the corresponding capacity contributed from CSN. The CSN material without any Sb provide 110 to 180 mAh/g capacity at current of 50-200 mA/g, as shown in Figure S3. In this work, evidently, the voltage profile exhibits two prominent discharge voltage plateaus, located at about 0.78 V ending with a capacity of about 216 mAh/g and 0.23 V ending with ~646 mAh/g, corresponding to the potassiation reaction of Sb to KSb_2/KSb and K_5Sb_4/K_3Sb, respectively; and two charge platforms were found at 0.64 V and 1.12V, which can be attributed to the extraction reaction of K from K_3Sb to Sb. Both the platform voltages and intensity of these two discharging/charging plateaus are in good agreement with the above-mentioned CV experimental results and calculated voltage profile. Figure S4 shows the first galvanostatic charge–discharge profile of the Sb@CSN anode at the same current and electrolyte. In the first charge/discharge cycle, Sb@CSN anode delivered an initial alloying and de-alloying capacity of 1049 and 640 mAh/g, respectively, leading to a low coulombic efficiency (CE) of 61%. It can be ascribed to the formation reaction of irreversible SEI layer on the surface of electrode, which is consistent with the reported results of Sb anode.[34] The quasi-thermodynamic equilibrium potential and K^+ diffusivity coefficient in Sb@CSN was measured using the galvanostatic intermittent titration technique (GITT) after 10 charge/discharge activation cycles, as indicated in Figure 4b.[35] The cell was discharged/charged at a current pulse of 100 mA/g for a duration period of 20 min, followed by an open-circuit stand for 120 min to allow fully relaxation back to its quasi-equilibrium potential. The quasi-equilibrium potential at different normalized K insertion/extraction levels are indicated by the blue dotted lines in GITT. The potential difference between end of charge/discharge and end of relaxation period represents the overpotential at the corresponding depotassiation/potassiation stage.[36] It can be observed that the overpotential for the depotassiation and potassiation process is as low as 0.15 V even at a high current of 100 mA/g, suggesting a fast K^+ diffusion in Sb@CSN material. Furthermore, the four successive GITT curves displayed in Figure S5 demonstrated a reversible potassiation/depotassiation process with a repeatable overpotential of as low as 0.15 V. These results strongly suggest that a fast and reversible depotassiation/potassiation dynamics can be achieved for the prepared Sb@CSN material in the 4M KTFSI electrolyte.

The cycle stability for the as-prepared Sb@CSN material was investigated in 1M KTFSI/EC+DEC (abbreviated as "1M KTFSI") dilute and 4M KTFSI concentrated electrolytes, respectively. Figure 5a presents the cycling stability and its corresponding CE during 100 cycles charge/discharge cycles at 100 mA/g in 1M and 4M KTFSI electrolyte. Specifically, the capacity of the Sb@CSN anode in 4M KTFSI electrolyte exhibits exceptional reversibility and cycling stability, maintaining a stable capacity of 551 mAh/g over 100 cycles with a high average CE of > 98% and a low capacity decay of 5.3% from 10th to 100th cycling; while the capacity of Sb@CSN material in 1M KTFSI electrolyte fades rapidly, only 286 mAh/g left at 100th cycles with fluctuant average CE of 95%. Similarly, the capacity of Sb@CSN anode in the common dilute 1M KPF_6/EC+DEC electrolyte also delivers a rapid capacity loss, with a discharge capacity of 603 mAh/g at 2nd cycling but only 256 mAh/g after 100 cycles, as indicated in Figure S6, suggesting the significant improvement of the electrochemical K-storage performance of Sb@CSN material by electrolyte optimization. Furthermore, the cycled Sb@CSN material also maintained complete sphere morphology with uniform Sb nanoparticles well-defined encapsulated in the carbon sphere (Figure S7), indicating excellent structure stability and efficient relief of the huge volume change during electrochemical reactions. These advanced properties should be ascribed to the well-designed carbon sphere matrix which can not only provide more space from its porous structures and defects to accommodate the volume change,[37] but also possess excellent flexibility and good adhesion to Sb nanoparticles to remarkably stabilize the Sb nanoparticles and reduce the strain during volume change process, protecting the CSN from crack.[38]

The impedance changes during charge/discharge cycles were measured using the electrochemical impedance spectroscopy (EIS). Figure S8 show the impedance of Sb@CSN before and after 100 cycles in

1M and 4M KTFSI electrolyte. It can be observed that the initial charge transfer resistance in 4M KTFSI electrolyte is higher than that in 1M KTFSI electrolyte, which can be attributed to the less wettability of concentrated 4M electrolyte to the Sb@CSN electrodes due to higher viscosity of 4M concentration electrolyte than that of 1M dilute electrolyte. After the 100 charge/discharge cycles, only a small increase in electron-involved reaction impedance is observed for Sb@CSN in 4M KTFSI electrolyte, while a large electron-involved reaction impedance increase is demonstrated in 1M KTFSI electrolyte. This result can be probably attributed to the formation of a thinner solid electrolyte interface (SEI) layer on Sb@CSN in the 4M electrolyte.

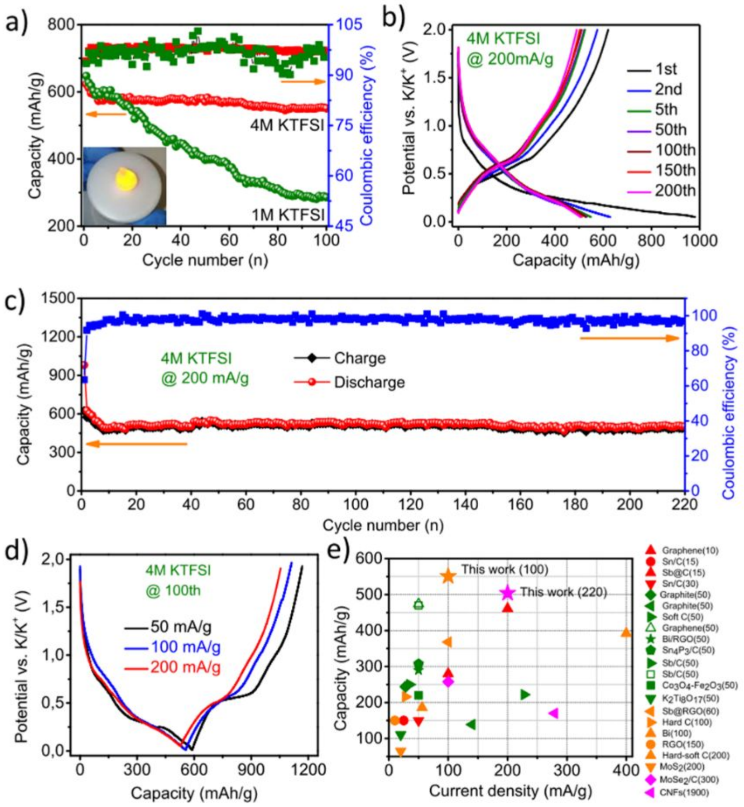

Figure 5 Electrochemical performance for Sb@CSN anode: a) cycling performance at 100 mA/g in 1M KTFSI and 4M KTFSI electrolyte (Inset: Lighting electronic candle with a coin cell in 4M KTFSI electrolyte after 100 cycles); b) charge/discharge curves and c) its corresponding cycling performance at 200 mA/g in 4M KTFSI electrolyte; d) The 50th charge/discharge curves under various current densities from 50 to 200 mA/g; e) Capacity comparison of Sb@CSN anode with previous reported anodes in PIBs, the numbers in brackets is the cycle numbers, the color code represents the cycling number range: red is < 50 cycles, olive is 50 cycles, orange is 50 to 200 cycles, magenta is > 200 cycles.

The long-term cycling stability of Sb@CSN composite in 4M KTFSI electrolyte at a high current density of 200 mA/g was also evaluated. As shown in Figure 5b-c, Sb@CSN at 200 mA/g in 4M KTFSI still provide a high discharge capacity of 626 mAh/g at 2nd cycle, which is very close to its theoretical capacity of 660 mAh/g (corresponding to the formation of K_3Sb). The capacity slightly decreases in the initial 10 cycles and then stabilizes at 504 mAh/g over 200th cycles. Correspondingly, the CE increases in the first 10 cycles and then approaches to a consistent value of 98%. These results manifest a reversible alloying-dealloying process between the formation of Sb and K_3Sb even at such a high current density. Furthermore, Figure 5d displays the charge-discharge profiles at various current densities after 50 cycles. The charge/discharge capacity only slightly decreases when increasing the current density from 50, 100 to 200 mA/g, along with a slight capacity decay from 589 mAh/g, 566 mAh/g to 530 mAh/g, respectively, which indicates excellent rate capability for the unique nanostructured Sb@CSN in 4M KTFSI electrolyte. Moreover, the voltage plateaus at various current densities show small differences, indicating only minor electrochemical polarization augment when increasing to a higher current.

Figure 5e and Table S1 compared the electrochemical performance of the Sb@CSN in 4M KTFSI electrolyte with reported K-ion battery anodes, including carbon-based anodes, metal alloy anodes, metal oxide (sulfide) anodes. It can be found that the Sb@CSN can achieve a high specific capacity of 551 mAh/g at 100 mA/g over 100 cycles with a capacity decay of 0.06% per cycle from the 10th to 100th cycling and 504 mAh/g at a high current density of 200 mA/g even after 220 cycles, which are much better than all reported K-ion battery anodes. Such excellent performance should be attributed to (i) the carbon sphere network which not only acts as the efficient conductive skeleton but also as the buffering for huge volume expansion of Sb nanoparticle during alloying/de-alloying reaction process, (ii) the small Sb crystallite with an average size of 14 nm which benefits to decrease K^+ diffusion distance, and (iii) the concentrated 4M KTFSI electrolyte employed here which can promote the formation of robust SEI to obtain good reversibility for the alloying/de-alloying reaction process.

The SEI compositions formed on Sb@CSN electrodes in 4M KTFSI and 1M KTFSI electrolytes were analyzed using X-ray photoelectron spectroscopy (XPS) coupled with Ar^+ etching technique. As demonstrated in Figure 6a and b, the signal of Sb element at the etching time demonstrated that the SEI in 4M KTFSI electrolyte is thinner than that in 1M KTFSI electrolyte (Table S2). Moreover, the SEI layer formed in 4M KTFSI electrolyte delivers an obviously lower C at.% and higher F at.% than that formed in the 1M KTFSI electrolyte, indicating that F-rich and inorganic-dominated SEI layer is preferred to be formed in the 4M concentrated electrolyte.[39] Figure 6c and d show the high resolution F1s XPS spectra for the electrode surface in 1M KTFSI and 4M KTFSI electrolyte, respectively. Two main signal peaks centered at 685.0 and 688.1 eV in the both electrolytes are assigned to F-K bonds and F-C bonds, respectively.[40] It can be found that at the outside surface (corresponding to etching time of 0 s) of Sb@CSN electrode in 1M KTFSI electrolyte, 69.20 at.% of F element exists as organic F-C bonds, suggesting an organic property of this surface. With the increasing etching time, the content of F-C bonds decreases gradually to 16.81 at. %, indicating the changes of SEI composition from organic sublayer to organic-inorganic hybrid sublayer. By contrast, the content of F-C bonds in the SEI layer formed in 4M KTFSI electrolyte is distinctly lower than that formed in 1M KTFSI electrolyte at all the etching times, resulting to a F-K dominated bonding property for the F element in the SEI layer. These results suggest a more inorganic SEI layer with abundant KF phase was formed in the concentrated 4M KTFSI electrolyte, well consistent with the previous report.[27] The high concentrated KTFSI electrolyte can weaken the solvent reduction and lead the reduction of KTFSI to mainly induce the formation of KF-rich SEI.

As demonstrated in Figure 6e, during the formation of SEI layer, K^+, $TFSI^-$ and solvent molecules should first reach to the electrode/electrolyte interface and then react irreversibly. It's much easier for the concentrated electrolyte to provide more $TFSI^-$ ions with abundant F element to reach the interface and then participate the SEI formation reaction in a faster kinetic way than in the 1M diluted electrolyte. Accompanied by the condition of concentrated K^+, a denser and thinner KF-rich SEI layer was preferred to be formed in 4M KTFSI electrolyte. Such a robust KF-rich SEI layer can not only protect the active materials from further reacting with the electrolyte, but also accommodate the volume change of Sb@CSN, thus leading to excellent K-storage performance for such a material. In addition, the high concentrated KTFSI also reduce the solubility of KF in electrolyte, further stabilizing the KF-rich SEI for excellent long-term cycling property.

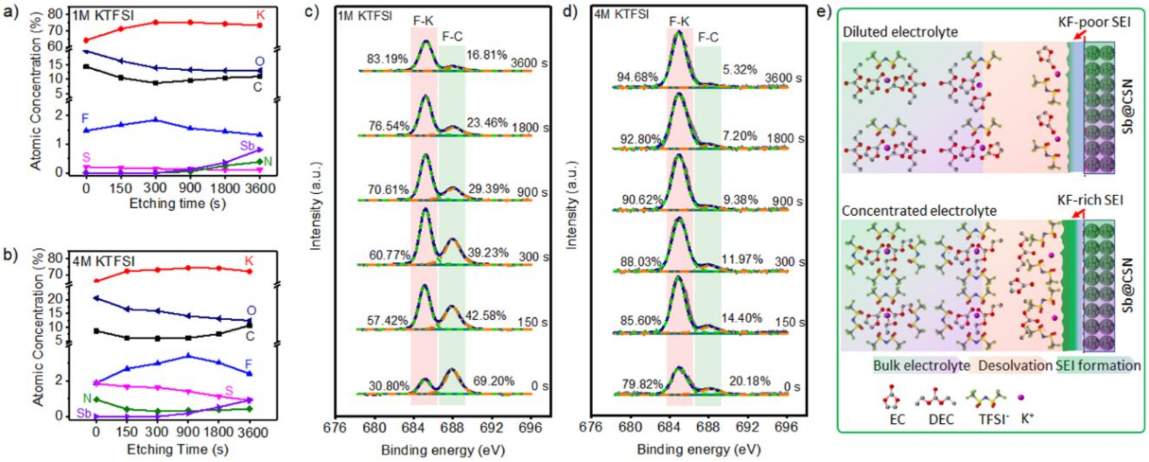

Figure 6a, b) Atomic percentage concentrations of different elements with increasing etching time and c, d) corresponding high-resolution F1s XPS spectra for the Sb@CSN electrode in a, c) 1M KTFSI and b, d) 4M KTFSI electrolyte; e) Illustration of the influence of dilute and concentrated electrolytes on the formation of SEI layer.

The high concentrated electrolyte can also reduce the flammability. The flammability of electrolytes was evaluated by soaking a piece of glass fiber membrane with 0.5 mL electrolyte and then immediately igniting it with butane lighter, as illustrated in Figure S9. The flame for the 4M KTFSI electrolyte is much smaller and darker than that of the dilute electrolyte and the same concentrated 4M $KClO_4$ electrolyte.

After the combustion, the glass fiber in 4M KTFSI electrolyte is black due to the fire retardation and incomplete combustion resulting from the stable and high concentrated KTFSI salt. By contrast, it is white for the dilute electrolyte, indicating the complete combustion of the electrolyte. For the 4M $KClO_4$ electrolyte, an obvious explosion can be observed due to the strong oxidization property of $KClO_4$. Therefore, the high concentrated 4M KTSFI electrolyte is suitable for highly secure batteries with less fire-severity and lower fire-catching properties.

Conclusion

In summary, Sb@CSN composite anode with evenly-distributed and small Sb nanoparticles confined in carbon sphere network has been successfully prepared for K-ion battery anode via unique electrospray-assisted strategy. Sb@CSN anode in the concentrated 4M KTFSI electrolyte shows a high reversible capacity of 551 mAh/g at 100 mA/g over 100 cycles with a capacity decay of 0.06% per cycle from the 10st to 100th cycling and 504 mAh/g after 220 cycles even at a high current density of 200 mA/g. It also shows excellent rate performance by providing 589 mAh/g at 50 mA/g and 530 mAh/g at 200 mA/g. Such a unique material in this concentrated electrolyte demonstrates one of the best capacity performances among all K-ion battery anode materials. These excellent K-storage performances should be ascribed to the formation of stable and robust KF-rich SEI layer along with the novel nanostructure of Sb nanoparticles uniformly encapsulated into the conductive carbon network. These discoveries provide valuable guidance for rationally developing advanced alloy-based electrode materials for high-performance PIBs applications.

Author Contributions

J. Z and Y. Y contributed equally to this work.

Acknowledgements

This work was supported by the US National Science Foundation Award No. 1438198. We acknowledge the support of the Maryland NanoCenter and its AIM Lab. The AIM Lab is supported in part by the NSF as a MRSEC Shared Experimental Facility. Y.Y, H. W and M. R. Z. are grateful for the support from the Multidisciplinary University Research Initiative (MURI) grant.

Conflicts of interest

The authors declare no competing financial interest.

References

1. B. Dunn, H. Kamath and J.-M. Tarascon, *Science*, 2011, **334**, 928-935.
2. D. Larcher and J.-M. Tarascon, *Nat. Chem.*, 2015, **7**, 19.
3. G. B. Haxel, J. B. Hedrick, G. J. Orris, P. H. Stauffer and J. W. Hendley II, *Rare earth elements: critical resources for high technology*, Report 2327-6932, 2002.
4. Y. Liang, Z. Chen, Y. Jing, Y. Rong, A. Facchetti and Y. Yao, *J. Am. Chem. Soc.*, 2015, **137**, 4956-4959.
5. N. Yabuuchi, K. Kubota, M. Dahbi and S. Komaba, *Chemical reviews*, 2014, **114**, 11636-11682.
6. V. Mathew, S. Kim, J. Kang, J. Gim, J. Song, J. P. Baboo, W. Park, D. Ahn, J. Han and L. Gu, *NPG Asia Mater.*, 2014, **6**, e138.
7. N. Recham, G. l. Rousse, M. T. Sougrati, J.-N. l. Chotard, C. Frayret, S. Mariyappan, B. C. Melot, J.-C. Jumas and J.-M. Tarascon, *Chem. Mater.*, 2012, **24**, 4363-4370.
8. C. Zhang, Y. Xu, M. Zhou, L. Liang, H. Dong, M. Wu, Y. Yang and Y. Lei, *Adv. Funct. Mater.*, 2017, **27**.
9. P. Padigi, J. Thiebes, M. Swan, G. Goncher, D. Evans and R. Solanki, *Electrochimi. Acta*, 2015, **166**, 32-39.
10. Y. Chen, W. Luo, M. Carter, L. Zhou, J. Dai, K. Fu, S. Lacey, T. Li, J. Wan and X. Han, *Nano Energy*, 2015, **18**, 205-211.
11. J. Zelang, X. Zhenyu, B. Clement, L. Zhifei and J. Xiulei, *Adv. Energy Mater.*, 2016, **6**, 1501874.
12. Z. Tai, Q. Zhang, Y. Liu, H. Liu and S. Dou, *Carbon*, 2017, **123**, 54-61.
13. Z. Jian, W. Luo and X. Ji, *J. Am. Chem. Soc.*, 2015, **137**, 11566-11569.
14. S. Komaba, T. Hasegawa, M. Dahbi and K. Kubota, *Electrochem. Commun.*, 2015, **60**, 172-175.
15. W. Luo, J. Wan, B. Ozdemir, W. Bao, Y. Chen, J. Dai, H. Lin, Y. Xu, F. Gu and V. Barone, *Nano Lett.*, 2015, **15**, 7671-7677.
16. Y. Liang, H. Tian, J. Repac, S.-C. Liou, J. Chen, W. Han, C. Wang and S. Ehrman, *Energy Storage Mater.*, 2018, **13**, 8-18.
17. I. Sultana, T. Ramireddy, M. M. Rahman, Y. Chen and A. M. Glushenkov, *Chem. Commun.*, 2016, **52**, 9279-9282.
18. Z. Li, J. Ding and D. Mitlin, *Acc. Chem. Res.*, 2015, **48**, 1657-1665.
19. K. T. Lee, Y. S. Jung and S. M. Oh, *J. Am. Chem. Soc.*, 2003, **125**, 5652-5653.
20. H. Kim, G.-S. Park, E. Kim, J. Kim, S.-G. Doo and J. Cho, *J. Electrochem. Soc.*, 2006, **153**, A1633-A1636.
21. J. Yin, M. Wada, S. Tanase and T. Sakai, *J.Electrochem. Soc.*, 2004, **151**, A583-A589.
22. W.-J. Zhang, *J. Power Sources*, 2011, **196**, 13-24.
23. J. Qian, Y. Chen, L. Wu, Y. Cao, X. Ai and H. Yang, *Chem. Commun.*, 2012, **48**, 7070-7072.
24. J. Sangster and A. Pelton, *J. Phase Equilibria*, 1993, **14**, 514-517.
25. W. D. McCulloch, X. Ren, M. Yu, Z. Huang and Y. Wu, *ACS Appl. Mater. Interface*, 2015, **7**, 26158-26166.
26. D. Aurbach, *J. Power Sources*, 2000, **89**, 206-218.
27. Y. Lei, L. Qin, R. Liu, K. C. Lau, Y. Wu, D. Zhai, B. Li and F. Kang, *ACS Appl. Energy Mater.*, 2018.
28. X. Wu, D. P. Leonard and X. Ji, *Chem. Mater.*, 2017, **29**, 5031-5042.
29. F. Su, X. Zhao, Y. Wang, J. Zeng, Z. Zhou and J. Y. Lee, *J. Phys. Chem. B*, 2005, **109**, 20200-20206.

30. H. Hou, M. Jing, Y. Yang, Y. Zhang, W. Song, X. Yang, J. Chen, Q. Chen and X. Ji, *J Power Sources*, 2015, **284**, 227-235.
31. Y. Yang, M. Romano, G. Feng, X. Wang, T. Wu, S. Holdren and M. R. Zachariah, *Langmuir*, 2018, **34**, 585-594.
32. Z. Jian, Z. Xing, C. Bommier, Z. Li and X. Ji, *Adv. Energy Mater.*, 2016, **6**.
33. A. Darwiche, C. Marino, M. T. Sougrati, B. Fraisse, L. Stievano and L. Monconduit, *J. Am. Chem. Soc.*, 2012, **134**, 20805-20811.
34. H. Hou, G. Zou, P. Ge, G. Zhao, W. Wei, X. Ji and L. Huang, *New J. Chem.*, 2017, **41**, 13724-13731.
35. W. Weppner and R. A. Huggins, *J. Electrochem. Soc.*, 1977, **124**, 1569-1578.
36. Y. Xu, C. Zhang, M. Zhou, Q. Fu, C. Zhao, M. Wu and Y. Lei, *Nat. Commun.*, 2018, **9**.
37. E. J. Ra, E. Raymundo-Piñero, Y. H. Lee and F. Béguin, *Carbon*, 2009, **47**, 2984-2992.
38. K. F. Chiu and P. Lai, *Mater. Sci. Engineer.: B*, 2018, **228**, 52-59.
39. X. B. Cheng, R. Zhang, C. Z. Zhao, F. Wei, J. G. Zhang and Q. Zhang, *Adv. Sci.*, 2016, **3**.
40. C. Xu, B. Sun, T. Gustafsson, K. Edström, D. Brandell and M. Hahlin, *J. Mater. Chem. A*, 2014, **2**, 7256-7264.

Broader Context

Recently, potassium-ion batteries (PIBs) have attracted increasing attention due to its low cost, abundant K resources, and low redox potential. However, conventional alloy PIB anodes still suffer from short cycling life due to huge volume changes during insertion/de-insertion of large-radius K ions. In this work, we significantly enhanced cycling stability of Sb alloy anodes by dispersing nano-Sb into porous sphere network (Sb@CSN) to migrate the volume changes of Sb@CSN and using highly concentrated 4M KTFSI/EC+DEC electrolyte to form a robust KF-rich solid electrolyte interphase on Sb@CSN. The synergistic effect of porous carbon substrate and robust SEI greatly enhance the electrochemical performance of Sb@CSN anode. The synergistic design of K-ion battery alloy anodes will inspire battery scientist to deeply understand the fundamental electrochemistry in PIBs and will be very useful in developing next generation of high-performance PIBs.